

This section of Journal of Materials Research is reserved for papers that are reviews of literature in a given area.

UNDERSTANDING WATER-OXIDE INTERFACES TO HARNESS NEW PROCESSES AND TECHNOLOGIES

Interaction of water with oxide thin film model systems

Martin Sterrer^{1,a)} , Niklas Nilius², Shamil Shaikhutdinov³, Markus Heyde³,
Thomas Schmidt³, Hans-Joachim Freund^{3,b)}

¹University of Graz, Institute of Physics, NAWI Graz, 8010 Graz, Austria

²Carl von Ossietzky Universität Oldenburg, Institut für Physik, 26111 Oldenburg, Germany

³Fritz-Haber-Institut der Max-Planck-Gesellschaft, Department of Chemical Physics, 14195 Berlin, Germany

^{a)}Address all correspondence to these authors. e-mail: martin.sterrer@uni-graz.at

^{b)}e-mail: freund@fhi-berlin.mpg.de

Received: 14 September 2018; accepted: 12 November 2018

The interaction between water and oxide surfaces plays an important role in many technological applications and environmental processes. However, gaining fundamental understanding of processes at oxide–water interfaces is challenging because of the complexity of the systems. To this end, results of experimental and computational studies utilizing well-defined oxide surfaces help to gain molecular-scale insights into the properties and reactivity of water on oxide surfaces. This is a necessary basis for the understanding of oxide surface chemistry in more complex environments. This review highlights recent advances in the fundamental understanding of oxide–water interaction using surface science experiments. In particular, we will discuss the results on crystalline and well-defined supported thin film oxide samples of the alkaline earth oxides (MgO and CaO), silica (SiO₂), and magnetite (Fe₃O₄). Several aspects of water–oxide interactions such as adsorption modes (molecular versus dissociative), formation of long-range ordered structures, and dissolution processes will be discussed.

Introduction

The interaction of water with surfaces is of major importance in many environmentally and technologically relevant processes, including electrochemistry, corrosion, atmospheric chemistry, weathering, materials science, solar water splitting, and catalysis. Thus, an enormous amount of research work, both experimental and computational, has been put into the understanding of water–surface interaction at different levels of complexity, from the single-molecule level to thin water films and bulk liquid water. Fundamental surface science studies with single-crystalline substrates and using advanced microscopic and spectroscopic surface science analytical methods have greatly contributed to the advancement of the understanding of water–solid interfaces as documented in a number of review articles [1, 2, 3, 4, 5, 6]. Among the surfaces studied, perhaps the most detailed information is nowadays available for single-crystalline metal substrates, for which the interaction with water is typically rather weak. Atomistic insight into the structural details of water clusters, chain-like structures, and two-dimensional networks formed at low temperature has

become available from scanning tunneling microscopy (STM) and infrared studies in combination with calculations using density functional theory (DFT). It is now well established that the nature of the substrate, its lattice spacing, and the subtle balance between molecule–substrate interaction and intermolecular hydrogen bond interaction have profound impact on the adsorption and arrangement of water molecules on metal surfaces [7, 8].

In contrast to metal surfaces, the chemistry at water–oxide interfaces is much more complex and atomic- and molecular-level understanding based on surface science investigations of these interfaces is just emerging. Generally, oxide surface termination [9, 10], acid–base properties [11], and the abundance of defects influence the adsorption mode of water, which can be molecular or dissociative. While early interpretation of water–oxide interaction was mainly based on the single-molecule interaction schemes, recent developments in computational and also experimental methodologies, e.g., in scanning probe techniques, have revealed a rich behavior of water on various oxide surfaces, which often depends on the water

coverage and is to a large extent determined by intermolecular interactions between molecular water and hydroxyl species. These interactions can, for example, lead to the stabilization of dissociated water in water clusters [12, 13] or give rise to the formation of extended two-dimensional water overlayers on oxides [14]. The understanding of the fundamental interaction of water with single-crystalline oxide surfaces under ultrahigh vacuum (UHV) conditions is the basis for more detailed investigations of oxides under environmentally more relevant conditions, e.g., ambient pressure and bulk-liquid water [5, 6, 15], where surface restructuring by enhanced hydroxylation and oxide hydrolysis, and possible dissolution of the oxide have to be taken into consideration.

Naturally, the surfaces of oxide bulk single-crystals are often chosen as substrates for studying water–oxide interaction. MgO(001) [16] and ZnO(10 $\bar{1}$ 0) [17] were the first examples where ordered water superstructures have been found, but TiO₂(110) is certainly the oxide that has attracted most attention [12, 18, 19, 20] because of its importance in photocatalytic water splitting. Alternatively to single-crystal bulk oxides, single-crystalline thin oxide films grown on metal single-crystals are used as substrates to avoid problems such as the segregation of bulk impurities or charging of insulating samples. Another problem that is circumvented by the use of thin oxide films is the often very small reflectivity of bulk oxide single crystals. This is particularly severe for infrared reflection absorption spectroscopy (IRAS) studies on bulk oxides, although much progress in the enhancement of signal-to-noise ratio has been achieved in the past years through improved instrumentation [21, 22, 23]. The number of thin film model systems that have been prepared and characterized in the past is enormous and covers almost all binary oxides existing in the bulk [24, 25, 26, 27]. In fact, the variability of thin film oxides is even larger than that of their bulk counterparts. The reason can be found in the much higher structural and compositional flexibility of oxide films of few-monolayer (ML) thickness, giving rise to a plethora of nonstoichiometric, strained, and polar structures that would be unstable in the bulk limit [24, 28]. Moreover, the geometric template effect of the substrate combined with different electronic coupling schemes is able to stabilize various unusual thin film configurations [26, 29].

In this article, we present an overview of recent surface science investigations into water–oxide interaction with metal-supported, single-crystalline thin oxide films as substrates, with focus on stoichiometric and bulk-like thin film oxides, carried out in the authors' laboratories. After a brief introduction into the structural properties of the oxide films discussed in this article (section “Structural properties of epitaxial oxide films”), we first present results about the formation of ordered

hydroxyl–water overlayers in UHV conditions on the alkaline earth oxides (MgO and CaO) and on magnetite (Fe₃O₄) [section “Ordered water structures on MgO(001), CaO(001), and Fe₃O₄(111)"]. Stable hydroxylation of MgO, monolayer FeO, and silica is difficult to achieve by simple water dosing in UHV. Therefore, section “Hydroxylation of thin oxide films” describes experimental results from hydroxylation studies carried out either at elevated pressure or by electron-assisted enhancement of hydroxylation. Finally, the focus of sections “Stability and dissolution of thin oxide films in aqueous solutions” and “Water–silica interface” is laid on the stability and dissolution of thin oxide films in aqueous solutions. The experimental results obtained with infrared and photoemission spectroscopy, temperature-programmed desorption, and scanning probe microscopies are supported by DFT calculations carried out by collaborators.

Structural properties of epitaxial oxide films

In the following, we will introduce some of the oxide films explored in our group, including binary ionic alkaline earth oxides with simple rock salt structure, bilayer silica, and magnetite (Fe₃O₄) as an example of a transition metal oxide, which can pose considerable challenges with respect to possible surface terminations. The structural properties provide the necessary basis for the subsequent discussion of their interaction with water.

MgO and CaO(100) films

The two rock salt oxides MgO and CaO are prominent model systems for chemically and catalytically driven surface science studies [30]. Their importance relies on several aspects. The rock salt oxides are characterized by particularly simple structural and electronic properties, i.e., a cubic unit cell with two atoms in the base, and a wide electronic band gap, respectively. As a consequence, they are highly accessible to theoretical calculations, but can also be prepared on a variety of squared atomic lattices with matching dimensions. Suitable supports for MgO (lattice parameter 4.2 Å) are Ag(001) [31], Fe(001) [32], and Mo(001) [33, 34], while CaO (lattice parameter 4.8 Å) is typically grown on Mo(001) [35]. Given the symmetry of the support, the rock salt layers develop their thermodynamically preferred (100) termination that is both structurally compact and charge compensated (Fig. 1). Attempts to stabilize alternative rock salt surfaces, e.g., the (111) termination, turned out to be challenging at least in an UHV environment [36]. This can be explained with the polar nature of the hexagonal rock salt plane, which needs to be compensated for either by surface reconstruction or by adsorption of charged ad-species [37, 38].

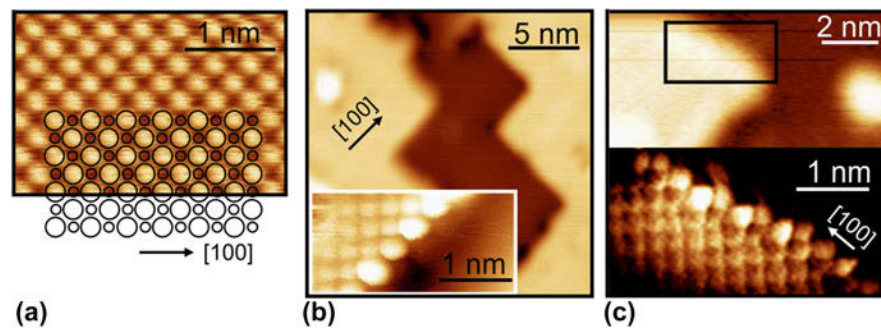


Figure 1: Low-temperature STM images of a 4-ML MgO(100) film on Ag(001), showing an atomically resolved terrace region (a), overview and atomically resolved images of a regular step edge (b), and an irregular step edge (c). Only one ionic sublattice of the MgO is resolved in the measurement.

The structural quality of MgO(001) and CaO(001) films is largely governed by a nonperfect lattice match with the support, which induces interfacial lattice strain and needs to be released by structural distortions in the film. Not surprisingly, relatively smooth and homogenous MgO(001) films have been grown on Ag(001) that features only 3% lattice mismatch with bulk MgO (Fig. 1) [31]. The film quality can be further improved by postannealing these layers at 773 K, followed by a slow cooling down procedure [39, 40]. The lattice mismatch due to Mo(001) is considerably larger (5.3%) and results in the development of a dense dislocation network to compensate the strain [34]. These line defects share a number of properties with the grain boundaries in realistic, polycrystalline MgO and shall thus been discussed in more detail [41].

The dislocation network has a periodicity of 55–60 Å with straight defect lines running parallel to the MgO[110] direction, as revealed with STM and GIXD in real and reciprocal space, respectively [42]. Along these directions, an extra Mg–O row that has no counterpart in the Mo support is introduced for 18 regular oxide rows. The result is a (19 × 19) MgO on (18 × 18) Mo coincidence lattice with square symmetry (Fig. 2). On the atomic scale, the dislocation network is associated with periodic switches of the interface registry, changing from O to Mg ions sitting atop the Mo atoms of the support. Energetically, the O–Mo registry is preferred, as reflected in a shorter interface binding length (2.3 Å) as compared to the Mg–Mo domains (3.5 Å) [43]. As the O–Mo and Mg–Mo regions lie on different height levels, the MgO film develops a considerable mosaicity, being reflected in a prominent splitting of the fundamental MgO spots in low-energy electron diffraction (LEED) data [42]. The modulated interface distance also produces a work function pattern on the MgO film, in which high work function values are found for the Mg–Mo registry, while values for the O–Mo domains are 1.5 eV lower. The difference can be explained with the suppressed electron spill-out from the Mo support at the compact O–Mo interface [44]. The reduced thermodynamic stability of the Mg–Mo registry finally leads to a higher concentration of

point defects in these domains [45]. The strain-induced dislocation network on MgO/Mo thin films gives rise to a spatially modulated adsorption behavior that can be exploited as template for the preparation of well-ordered ensembles of metal particles [43].

With increasing oxide thickness, additional defect types develop next to the dislocation network (Fig. 2). Prominent defects at 10 ML film thickness are screw and edge dislocations, the latter being aligned with the nonpolar MgO[100] direction [42]. Also point defects, in particular oxygen vacancies, become more abundant. They mostly locate along step edges, where the atomic coordination is reduced with respect to atoms embedded in a compact terrace. The lattice position of oxygen vacancies has been thoroughly characterized by angle-dependent EPR measurements in combination with scanning probe techniques [46, 47].

CaO thin films have been prepared on Mo(001) substrates as well. Here, the impact of the lattice mismatch is even larger (8.1%) and triggers an alternative strain-relaxation scheme at the interface. To reduce compressive strain, Mo ions are incorporated into the first Ca–O layer in a highly ordered fashion. This becomes evident in a sharp (2 × 2) superstructure, seen both in electron diffraction and in STM measurements of the first oxide layers (Fig. 3) [35]. Driving force for the formation of a Ca–Mo mixed oxide at the interface is the lower Mo–O binding length (1.9 Å) with respect to the Ca–O bulk value (2.4 Å). Moreover, the mixed system experiences substantial thermodynamic stabilization, arising from the large oxidation enthalpy of Mo [48]. Given a high diffusion barrier, the influx of Mo atoms diminishes with increasing oxide thickness and formation of mixed Ca–Mo oxide terminates at about 4 ML. Beyond this limit, essentially unstrained CaO rock salt islands evolve on the surface and merge to a flat, (001)-terminated film at 10–15 ML total thickness (Fig. 3). However, even in this stage Mo ions can be detected in the rock salt lattice, distinctively affecting the chemical activity of the CaO/Mo(001) systems, for example in oxygen activation [49].

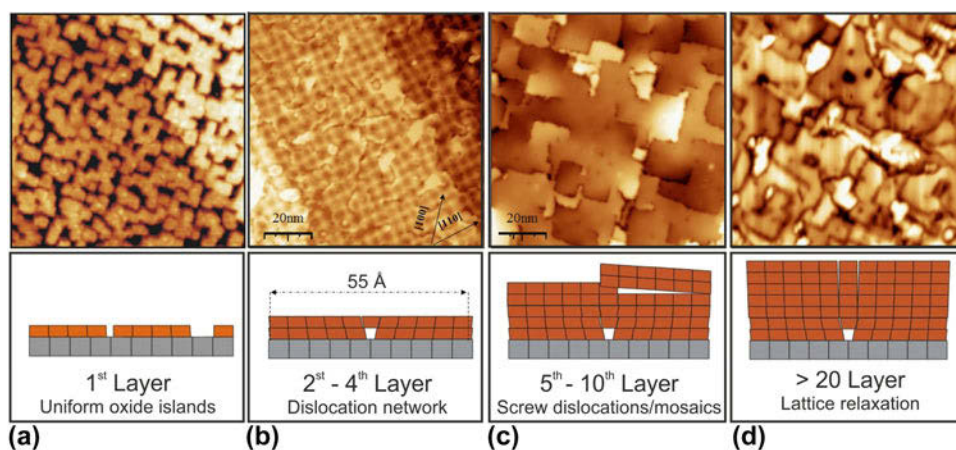


Figure 2: STM images showing several states of strain relaxation in MgO thin films on a Mo(001) support ($100 \times 100 \text{ nm}^2$, $V_s = 4.0 \text{ V}$) (a) Submonolayer coverage with square-shaped MgO islands. Their size is controlled by the interfacial lattice strain. (b) 3 ML thick film displaying a squared coincidence lattice. (c) 7 ML thick film characterized by wide, atomically flat terraces, separated by edge and screw dislocations. (d) 18 ML film with bulk-like lattice parameter. The image quality in (d) is degraded due to the vanishing conductivity of thick MgO layers.

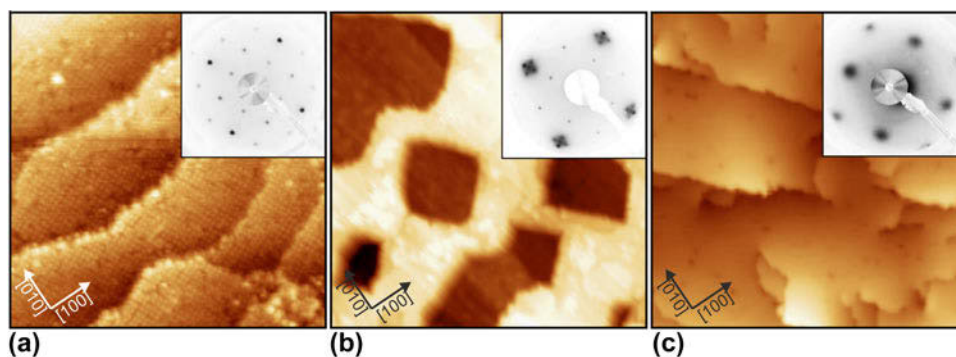


Figure 3: STM topographic images of CaO films of increasing thickness (a): 3 ML ($25 \times 25 \text{ nm}^2$), (b) 5 ML ($30 \times 30 \text{ nm}^2$), (c) 10 ML ($100 \times 100 \text{ nm}^2$). The insets depict the associated LEED patterns, showing a (2×2) superstructure in (a), a mixture of (2×2) and faceted CaO (1×1) in (b) and pristine CaO (1×1) in (c).

Silica film

The alkaline earth oxides discussed above represent a class of oxides, which tends to crystallize in a well-defined simple lattice driven by the Madelung potential of the highly ionic system. Even such prototypical ionic systems exhibit considerable structural complexity, in particular with respect to the defect structure. Another level of complexity arises if the system under consideration tends to form amorphous structures.

The prototype for amorphous network structures is silicon dioxide. This material is the simplest and most common type of glass. Many elements and compounds can form glasses and some of the oldest man-made objects found are made from glassy materials [50, 51, 52]. Glass materials and especially silicates are relevant in nature and various branches of modern technologies, e.g., in semiconductor devices, in optical fibers, and as a support in industrial catalysis [53]. To push this material class forward and to understand chemical reaction at surfaces, we should characterize their structures and properties at the atomic scale.

Zachariasen's postulates laid the foundation to the so-called "random network theory" 80 years ago to explain the structure of amorphous materials [54]. Due to the comparable mechanical properties of amorphous and crystalline materials, he assumed that the bonding forces between the atoms in the two phases should be essentially identical. The lack of periodicity and symmetry are the main features that distinguish a glass from a crystal. Early on, it had been suggested that tetrahedral atomic configurations were required to form glasses. Zachariasen used these predictions to sketch an atomic picture of a glass. In his paper, he reduced the three-dimensional (3D) picture into a two-dimensional (2D) analogy [Fig. 4(b)]. For silicon dioxide, the simplest structural unit in the 3D case is a SiO_4 tetrahedron. If the complexity of the system is reduced from 3D to 2D, the simplest structural unit for silicon dioxide changes from the SiO_4 tetrahedron to a SiO_3 triangle. The blue circle in Fig. 4 marks the SiO_3 building unit. The SiO_3 triangles are linked to each other as individual

building blocks at fixed 180° angles, corresponding to a crystalline material. This creates long-range order and periodicity. If the angle between these structural units varies, the building blocks can develop an extended network with rings of different sizes. As can be seen in Fig. 4(b) (bottom), the uniform structural units are linked to each other at apparently random angles. Zachariassen drew a 2D diagram in which trigonal units are linked together to create the amorphous network. Due to the large variety of Si–O–Si angles which bridge two neighboring building units, the glass structure lacks long-range order.

We have developed a recipe to grow thin silica bilayer films on Ru(0001). This film system verifies the complex atomic arrangement of the random network theory with striking similarity. The observed protrusions at atomic separations in the STM images shown in Figs. 4(a) and 4(c) are arranged in propeller-shaped structures. By comparison with Zachariassen's model and based on this propeller symmetry, the protrusions can be assigned to Si atoms [green balls in Figs. 4(a) and 4(c)]. Such propeller-shaped units have been separately marked in Fig. 4. Here, a Si-sensitive contrast is observed and the position of the O atoms has been calculated based on the Si coordinates. In this way, the 2D model of the topmost O and Si atoms has been completed. Note that a modified tip termination can make the O instead of the Si positions visible [55]. This silica film develops crystalline structures [56], but also verifies Zachariassen's predictions of a vitreous random network for a glass [57].

Besides the separate characterization of each phase, also interface structures between crystalline and amorphous phases have been addressed [58]. In the glass community, there has always been a controversy about how crystalline and vitreous phases are connected to one another. From the experimental point of view, a real-time observation at the atomic scale of an active front during a glass transition process is not currently feasible. But a static image of such an interface region can be gained. For further details, see Ref. 58.

Furthermore, it should be mentioned that silica bilayer films can be grown on a number of substrates [57, 59, 60, 61],

which leaves room for tuning the properties of these films, but also shows that these films resemble a completely new material class of its own.

With these experiments, a clear image of an amorphous material has been obtained which allowed for the first time the derivation of atomic sites and a detailed analysis from real space coordinates. The text book example of the amorphous silica structure proposed by Zachariassen in 1932 has thereby finally been verified. Also, Mo(112) and Pt(111) substrates have been used to prepare thin silica films. Given the stronger interface interaction in this case, those films are generally crystalline and mostly comprise regular networks of six-membered –Si–O– rings.

Iron oxide films

The oxide films discussed so far are simple in the sense that the oxidation state of the constituents is well defined. This restriction is lifted if transition metal oxides are considered. In addition, the ability to form oxides with different formal oxidation states of the cations is associated with changes in the bulk crystal structures. With respect to the atomic structure of the surfaces observed for different oxides, the surface termination becomes a central aspect.

Iron oxides have a wide range of technological applications, ranging from magnetic devices to heterogeneous catalysis [62, 63]. This class of materials exhibits rather different magnetic or conducting properties [64] depending on their crystal structures, which is strongly determined by the way of preparation. The morphology and termination of the oxide film have a strong influence on the chemical properties and are, therefore, a subject of intense studies [65, 66, 67, 68, 69].

Figure 5 briefly sketches the crystal structures of FeO (wustite), Fe₃O₄ (magnetite), and α-Fe₂O₃ (hematite). α-Fe₂O₃ crystallizes in the corundum structure with a hexagonal unit cell. Along the [0001] direction, the O anions form a close-packed hcp sublattice with ABAB stacking. The Fe³⁺

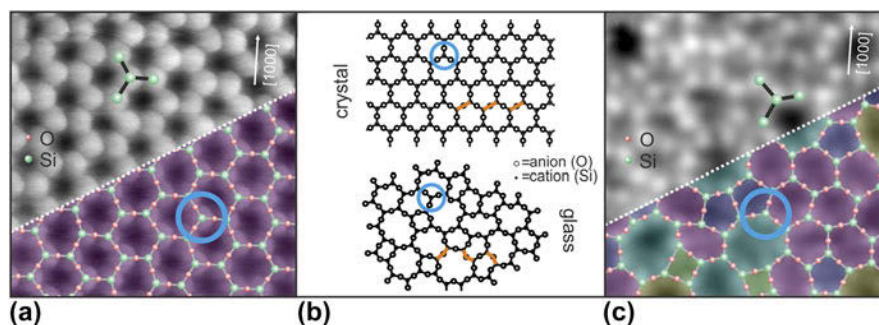


Figure 4: Atomically resolved crystalline and vitreous regions of the thin silica film by STM [the scan area of image (a) and (c) is 3.5 × 3.5 nm] [55]. An atomic model of the topmost layer of the silica film is superimposed onto the lower section of the images in (a) and (c) (green balls: Si atoms, red balls: O atoms). Zachariassen's scheme of crystalline and glass network structures is given in (b) for comparison [54].

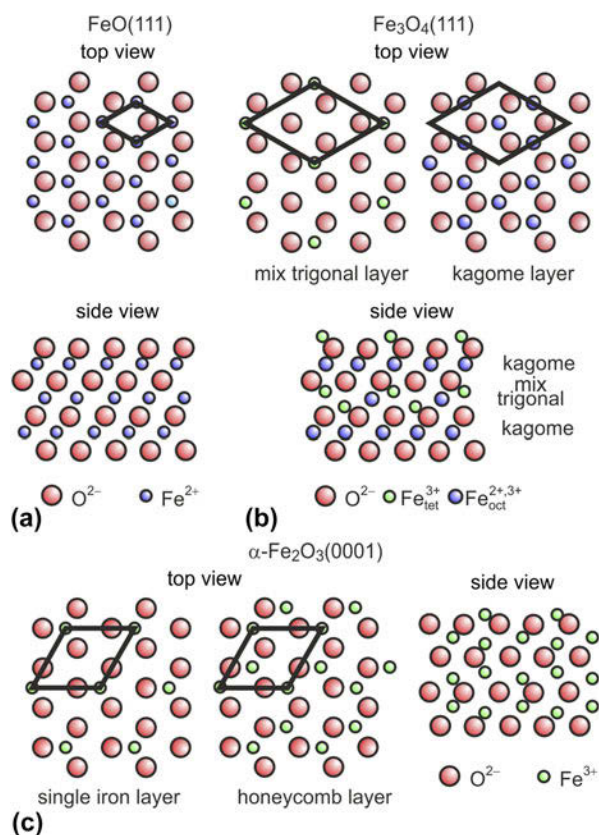


Figure 5: Models of iron oxides structure for (a) wustite (FeO), (b) magnetite (Fe₃O₄), and (c) hematite (α-Fe₂O₃) (adapted from Ref. 65).

species between these layers are arranged in honeycomb ($\sqrt{3} \times \sqrt{3}$)R30°-like layers. Fe₃O₄ crystallizes in the inverse spinel structure. The O anions form a close-packed fcc sublattice (ABC stacking along the [111] axis of the lattice) with Fe²⁺ and Fe³⁺ cations located in the interstitial sites. The O planes are similar to those in α-Fe₂O₃. Between the close-packed planes of oxygen ions, either one Kagomé or three hexagonal (mix-trigonal) Fe layers alternate. Both ion sublattices are arranged in a (2 × 2)-like fashion on the close-packed oxygen layer. FeO crystallizes in the rock salt structure; hence, the O and Fe (111) planes form ideal 2D hexagonal lattices with a cubic ABC stacking sequence along the [111] direction. For a more detailed overview of these different crystalline structures and the growth of iron oxide films on Pt(111), see Weiss and Ranke [65].

Hematite films will not be further discussed in this review. FeO(111) forms, when grown on Pt(111), well-ordered monolayer films with the Fe layer in direct contact with the Pt(111) substrate, and a close-packed oxygen layer on top. A peculiar feature of the monolayer FeO(111)/Pt(111) films is the periodic variation in the interface structure imposed by the lattice mismatch between FeO(111) and Pt(111). This leads to the formation of a Moiré superlattice featuring three high-symmetry rotational domains with Fe atoms either at on-top,

hcp, or fcc stacking position with respect to the underlying Pt (111) interfacial atoms. Polarity compensation is achieved in the thin film system by charge transfer at the interface and a strong inward relaxation of the oxygen layer. This and the fact that the FeO(111) film is oxygen terminated render the film quite unreactive at UHV conditions.

Fe₃O₄(111) films of about 10 nm thickness on Pt(111) are prepared by repeated cycles of Fe deposition at room temperature and oxidation at elevated temperatures, after one complete FeO layer was formed initially [65]. In each cycle, between 5 and 10 ML of Fe is deposited, oxidized at 1×10^{-6} mbar of O₂ and annealed at 900 K for 5 min. Upon cooling, the oxygen pressure is reduced only after the temperature is below 500 K. By following this procedure, the Pt(111) crystal is completely covered by an Fe₃O₄ film [Fig. 6(a)].

The LEED pattern of the film matches perfectly the one described in the literature [70]. The film consists of terraces up to 100 nm, most of them with polygonal shape. As seen in low energy electron microscopy (LEEM), the step density increased after every deposition and oxidation cycle, especially above 20 nm film thickness. However, the film can be smoothed if the final oxidation treatment is performed at an elevated temperature of about 1000 K. Here, it is necessary that the film is completely closed and thicker than 7 nm; otherwise, the 1000 K annealing step leads to dewetting. A subsequent thermal flash in UHV does not produce further morphological changes, but improves the homogeneity of the surface structure.

Magnetite crystallizes in an inverse spinel structure with space group *Fd3m*, while the Pt substrate exhibits a fcc structure with space group *Fm3m*. Therefore, the Fe₃O₄ islands created by initial nucleation on a clean Pt(111) surface may coalesce with improper stacking [71, 72] and form a complete film with two twin domains rotated by 180°. Dark-field LEEM studies using the (1/2; 0) and (0; 1/2) spots show a predominance of one rotational domain [69]; the coverage ratio for

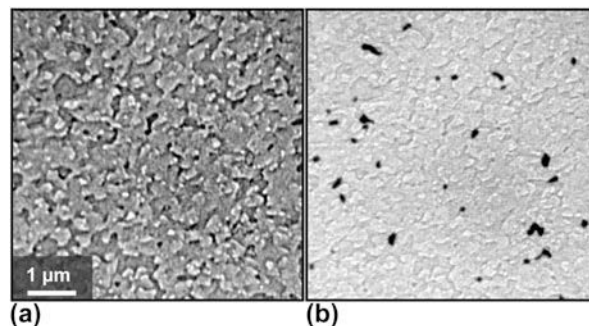


Figure 6: Morphology of a well-prepared Fe₃O₄ film, completely covering the Pt(111) support. Both LEEM images show the identical surface area in (a) bright- and (b) dark-field imaging mode, utilizing the (0; 0) and the (1/2; 0) diffraction spots, respectively. The contrast is caused by the morphology. Additionally, domains rotated by 180° become visible as dark areas in the dark-field image [69].

these rotational domains ranges between 75%/25% and 98%/2%, depending on the preparation condition. Figure 6(b) shows a dark-field LEEM image visualizing the two rotational domains as dominating bright and small black areas. This preponderance is maintained even after subsequent cycles of Fe deposition and oxidation. On average, the rotational domain size is larger than the terrace width; some of the domains are even several μm wide. A comparison between dark-field and bright-field LEEM images shows that the rotational domains preferentially develop in accordance to step bunches of the substrate, providing a partial correlation between substrate morphology and crystallographic inhomogeneities.

We note that, although the (111) surface of Fe_3O_4 (magnetite) has been investigated for more than twenty years, substantial controversy remains in the literature regarding the surface termination proposed from structural and adsorption studies [69, 73, 74, 75]. It appears that this issue is now solved. Our recent study [76] showed that IRAS and TPD experimental results of CO adsorption can only be explained under the assumption that the $\text{Fe}_3\text{O}_4(111)$ surface is terminated by a $1/4$ monolayer of tetrahedrally coordinated Fe^{3+} ions on top of a close-packed oxygen layer in full agreement with previous I/V LEED studies. However, surface defects play a crucial role in adsorption and may dominate chemical reactions on $\text{Fe}_3\text{O}_4(111)$ when exposed to the ambient.

Interaction of water with oxide films

In this section, we review some of the results obtained with the thin oxide films introduced in section “Structural properties of epitaxial oxide films” with regard to water interaction, showing how a combination of different methods allows us to gain atomistic insight into the energetics of adsorption processes as well as the nature of the surface species.

Ordered water structures on $\text{MgO}(001)$, $\text{CaO}(001)$, and $\text{Fe}_3\text{O}_4(111)$

A comparison of water adsorption on the (001) surfaces of the alkaline earth oxides is interesting because they all have the same structure (fcc), but different lattice constants and basicity, which is expected to strongly influence the mode of water adsorption (molecular or dissociative) and the ability to form long-range ordered 2D structures. While monolayer water adsorption on MgO has extensively been studied in the past both experimentally and theoretically and is now well understood, details about the higher alkaline earth oxides such as CaO and SrO have only recently become available. It is well established that a single water molecule adsorbs molecularly on the $\text{MgO}(001)$ surface, but may dissociate, even under UHV conditions, on defects such as low-coordinated cation–anion

pairs on step edges. By contrast, single-water-molecule adsorption is dissociative on CaO and SrO and involves considerably higher adsorption energies, as shown in Fig. 7(a), which displays the computed adsorption energy, E_{ads} , for water on the various oxides [77]. The dissociated monomer consists of a dynamic ion pair with the hydroxyl group (“free” OD, OD_f) adsorbed in bridge position between two cations and the proton transferred to a nearby oxygen ion [“surface” OD, O_sD , Fig. 7(c)] [78].

An interesting trend is seen for increasing water coverage, i.e., for increasing the number of water molecules per (3×4) unit cell used in the calculations: While the adsorption energy increases with increasing coverage for MgO and 2D monolayer structures are found to be the most stable water adsorption states, the calculated E_{ads} for water on $\text{CaO}(001)$, although very similar in the entire coverage range, is highest for 1D structures. For SrO, isolated and dissociated monomer and dimer species are expected to be more stable than the oligomer species. Experimentally, evidence for the 2D ordered arrangement of the water monolayer on MgO has been provided by diffraction and scattering methods more than 20 years ago [16, 80]. More recently, the presence of 1D water structures was proved by STM upon water adsorption on thick $\text{CaO}(001)$ films at room temperature [Fig. 7(b)] [77, 79], and the confirmation of the dynamic ion pair nature of a single, dissociated water molecule, as well as the stability of dimer species, on SrO has been obtained by STM on SrO-terminated $\text{Sr}_3\text{Ru}_2\text{O}_7$ [81].

Generally, diffraction methods and STM do not allow the positions of the individual water species and their chemical nature (molecular or dissociated) within the 1D and 2D water structures found on $\text{MgO}(001)$ and $\text{CaO}(001)$ to be determined, and one has to resort to high-level computations and spectroscopic methods to learn more about the molecular-scale details of these structures. Whereas electron spectroscopies can provide information about the presence of dissociated and molecular water, which, for example, has provided first experimental proof for the existence of mixed molecular/dissociated water molecules in the water monolayer on $\text{MgO}(001)$ [82], comparison of experimentally measured and computationally obtained frequencies of water and hydroxyl vibrations yields additional information about the structural details.

The latter approach has been used to identify and confirm the structural models of the 2D water monolayer on $\text{MgO}(001)$ [14] and of the 1D chain structures found by STM on CaO (001) [77, 79]. Figure 8 shows the experimental IRAS spectra (top panel) for the water monolayer prepared on MgO [Fig. 8 (a)] at low temperature (160 K) and for the water chain structures prepared on $\text{CaO}(001)$ at room temperature [Fig. 8 (b)], and the corresponding calculated anharmonic vibrational

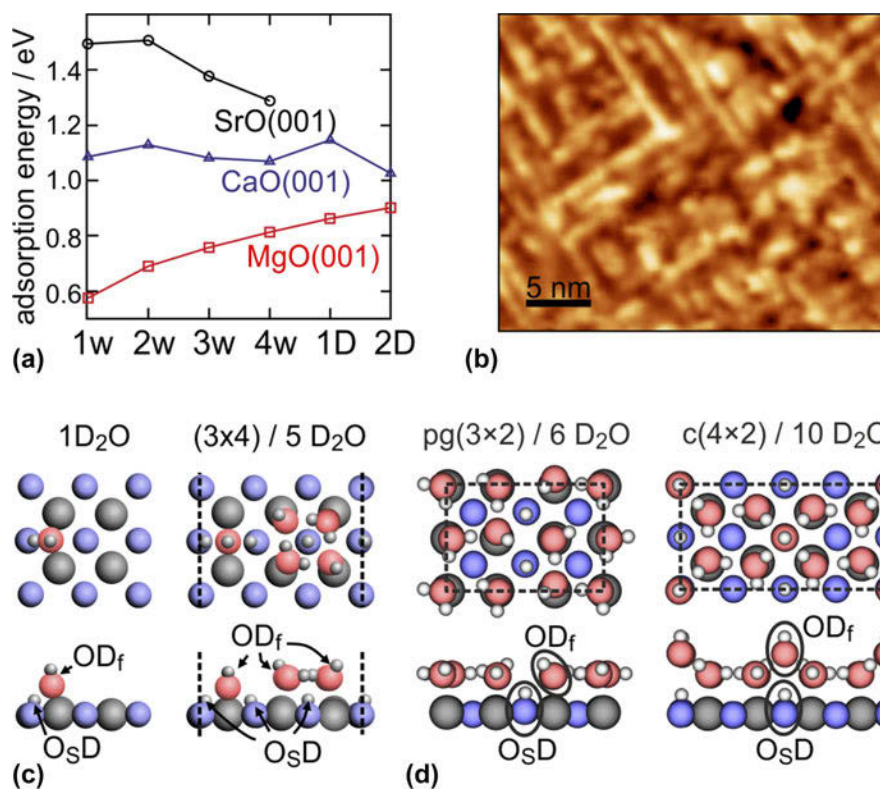


Figure 7: (a) Calculated adsorption energy per water molecule on CaO(001), MgO(001), and SrO(001) for increasing water coverage [1w, etc.: 1 water molecule per (3 × 4) unit cell; 1D: 1-dimensional water–hydroxyl structures; 2D: 2-dimensional water–hydroxyl structures]. (b) RT-STM image (30 × 25 nm²) of 1-dimensional water chains formed on CaO(001). (c) Most stable structures of the dissociated water monomer on CaO(001), the 1-dimensional chain structure on CaO(001), and the two most stable ordered 2-dimensional water phases [pg(3 × 2) and c(4 × 2)] on MgO(001). (Reprinted with permission from Refs. 14, 77, and 79. Copyright (2011, 2015, 2016) American Chemical Society.)

spectra (lower panel) (note that the experiments and calculations were performed with D₂O instead of H₂O). The experimental spectra are qualitatively similar and exhibit reasonably narrow bands in the range 2600–2750 cm⁻¹ and broad absorption between 2000 and 2500 cm⁻¹. The individual spectral contributions can be assigned based on the good agreement between the experimental and calculated spectra of the most stable structures shown in Fig. 7(c). For both, the MgO(001) and CaO(001) surfaces, the ordered water structures are comprised of dissociatively and molecularly adsorbed water. In the case of MgO, two ordered structures with different water coverage, the high-coverage c(4 × 2) and the low-coverage pg(3 × 2) structure, coexist at 160 K and can be distinguished based on the different frequencies of the O_SD groups [14]. Note that, due to the metal surface selection rule, the molecular water species, which are oriented almost parallel to the surface in both structures, give rise to only weak absorption signals. In fact, they do not contribute to the IR spectrum of the pg(3 × 2) structure. In the case of the c(4 × 2) structure, the molecular water species stabilize the protruding OH_f group, and combinations of their symmetric and antisymmetric stretch vibrations lead to signal contributions in the 2100–2400 cm⁻¹ spectral range,

which are detected in the experiment as a broad featureless absorption. Molecular water species in the 1D chain structure on CaO(001) are also oriented parallel to the surface and contribute only little to the IR signal on the thin film sample. The more defined signals for water on CaO(001) originate from OH_f (at highest wave number) and O_SD groups from dissociated water. Note that the O_SD groups in the 1D chain structure on CaO(001) are spectrally much more separated than in the 2D structures on MgO because the strength of hydrogen bonding between O_SD groups and OD_f groups is markedly different in the tetramer unit and in the linker unit, see Fig. 7(c) [77].

The combined experimental and computational analysis of water adsorption on the alkaline earth oxides has not only contributed to a better understanding of the molecular details of water structures, but additionally allows conclusions about the evolution of different structures on the surfaces to be drawn. Dissociation of a single water molecule is favored and involves larger adsorption energies when going from MgO to SrO. This can be explained by the increasing lattice constant and substrate flexibility when descending the AEO series [11]. Additionally, the subtle balance between intermolecular and molecule–surface interactions determines also the stability of

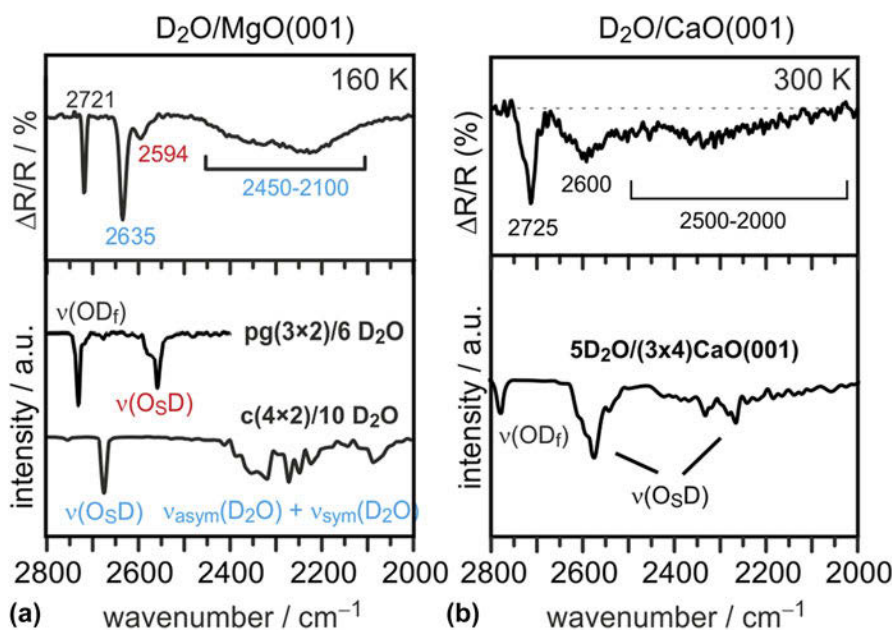


Figure 8: Experimental (top) and computed (bottom) IR spectra of the 2-dimensional water (D₂O) structures on MgO(001) (a) and the 1-dimensional water (D₂O) chain structure on CaO(001) (b). (Reprinted with permission from Refs. 14, 77, and 79. Copyright (2011, 2015, 2016) American Chemical Society.)

higher coverage structures: Two-dimensional ordered structures are stabilized on MgO(001) because of the weak interaction between water and the MgO surface and the favorable dimension of the MgO lattice parameter, which allows a strong hydrogen bonding network between adsorbed water and hydroxyl species to be established. The CaO lattice is slightly too large to enable the formation of a hydrogen-bonded network, and the water structures therefore collapse into a 1D configuration at low coverage. Similar 1D assemblies become stable also on MgO(001) when its lattice parameter is artificially increased to reduce the effect of intermolecular coupling. In contrast on SrO(001), the water residuals are always too far away to form uniaxial or 2D hydrogen-bonded arrangements [77].

The results presented for the alkaline earth oxides demonstrate that not only the acid–base properties of the oxide surface, but also the lattice parameter and hence the ability to form hydrogen bonds between neighboring water molecules and hydroxyl groups have a major impact on the adsorbed water structures. In a further example, vibrational spectroscopy combined with DFT calculations has been used to study the adsorbed water structures formed on well-ordered Fe₃O₄(111). Analysis of previous studies on water adsorption on Fe₃O₄(111), both for single crystals and thin films, revealed some controversy in the literature which most likely originated from the experimental difficulties of preparing well-defined, clean, and uniform surfaces. Iron oxide single crystals often expose several coexisting surface structures. Apparently, thin films grown on a metal substrate are more uniform. However, defect

structures are still difficult to control and characterize. In addition, surface preparation and even vacuum conditions may play an important role due to adventitious adsorption of residual (CO, water, CO₂) gases in the background.

Figure 9(a) shows a series of TPD spectra obtained upon water exposure at 140 K. The peak at 160 K is straightforwardly assigned to the formation of an amorphous solid water (ASW) film. Desorption peaks at 200, 225, and 255 K are sequentially populated following first-order desorption kinetics, whereas the broad signal above 275 K shows characteristics of second-order desorption typical for associative desorption of dissociated water species. The small feature at 375 K is most likely due to adsorption on defect sites. These desorption spectra differ considerably from the previously reported ones in Refs. 83, 84, 85 only showing smooth desorption in the 200–300 K region. Using water adsorption on the clean Pt(111) surface as a reference, the saturated amount of water adsorbed on Fe₃O₄(111) prior to the ASW film formation (θ_{\max}) is found to be 2.3 ± 0.2 ML (where 1 ML is defined as one H₂O molecule per Fe₃O₄(111) unit cell exposing one Fe ion, i.e., 3.2×10^{14} cm⁻²).

The Redhead analysis [86] using the standard prefactor of 10^{13} s⁻¹ yields desorption energies ranging from 50 kJ/mol for the peak at 200 K up to 95 kJ/mol for the peak at 375 K. A “leading edge” analysis [87, 89], that does not require assumptions on the pre-exponential factor, resulted in an energy of 68 kJ/mol at low coverage that gradually decreased with increasing coverage as shown in Fig. 9(b). Finally, we used inversion analysis of the Polanyi–Wigner equation for first-order desorption kinetics [90], which resulted in a desorption

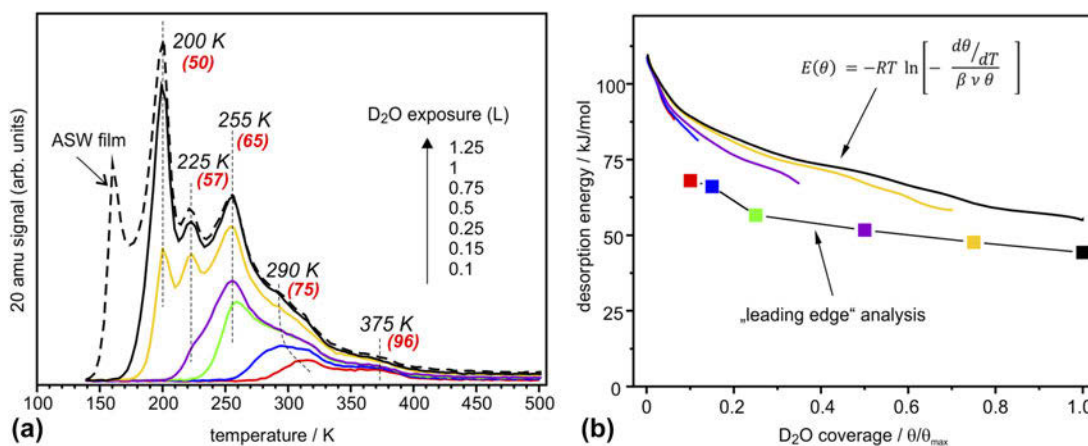


Figure 9: (a) TPD spectra of D₂O (20 amu) adsorbed at 140 K at increasing exposures as indicated. The heating rate was 3 K/s. At the highest exposure, the formation of an ASW film sets in. The numbers in parenthesis show desorption energies obtained by the Redhead formalism [86] using a prefactor $\nu = 10^{13} \text{ s}^{-1}$. (b) Desorption energy as a function of water coverage obtained by a “leading edge” analysis [87] and by inversion analysis of the Polanyi–Wigner equation with a prefactor $\nu = 10^{13} \text{ s}^{-1}$. Water coverage is normalized to the maximum obtained before the ASW related peak sets in. (Reproduced from Ref. 88.)

energy (E): $E(\theta) = -RT \ln \left[-\frac{d\theta/dT}{\beta \nu \theta} \right]$ where β is the heating rate, ν is a prefactor, and $\theta(T)$ is a temperature (or time)-dependent coverage, which is determined by integration of the desorption curve. In this analysis, each spectrum can be transformed into a coverage-dependent energy curve, all plotted in Fig. 9(b), for $\nu = 10^{13} \text{ s}^{-1}$. Some deviation between the curves may be indicative of kinetic effects. These results show again that the desorption energy decreases with increasing coverage, most markedly in the low-coverage regime ($\theta < 0.2$).

The differential heats of adsorption of D₂O on Fe₃O₄(111) measured by single-crystal calorimetry [91] revealed basically the same behavior. The measured adsorption energies and their coverage dependence are fully consistent with the TPD results, suggesting that the adsorption and dissociation of water is reversible under the conditions studied.

Well-resolved desorption peaks observed in the TPD spectra [Fig. 9(a)] indicated desorption of species with discrete adsorption energies that desorb almost simultaneously in time, which in turn implies a certain degree of ordering at the surface. Indeed, a LEED study [88] revealed additional spots identified as Fe₃O₄(111)-(2 × 2) structure, which appeared if the sample was exposed to saturation amounts of water at temperatures between 200 and 255 K, i.e., in the range where sharp desorption peaks are observed.

To elucidate the adsorption mechanism, we performed IRAS studies, in particular using isotopic labeling of oxygen that allows to discriminate oxygen in water (OD_f) and hydroxyl species involving oxygen on the oxide surface (O_sD). The results showed that (beside the lowest-coverage band at 2681 cm⁻¹ being assigned to adsorption on defects) the IR bands at 2718 cm⁻¹ and 2688 cm⁻¹ are associated to OD_f and O_sD species, respectively, both resulting from water dissociation [Fig. 10(a)].

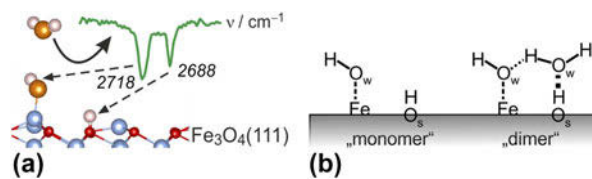


Figure 10: (a) Assignment of OD vibrational modes on Fe₃O₄(111). (b) Schemes for the dissociatively adsorbed water monomer (left) and water dimer (right).

DFT calculations substantiated these conclusions. Specifically, the computed adsorption enthalpy of the monomer is -102 kJ/mol and the corresponding OD bands are 2736 and 2699 cm⁻¹, respectively. These act as an anchor for water molecules to form a dimer complex [Fig. 10(b)] which self-assembles into an ordered (2 × 2) structure at increasing coverage. At high coverages, dimers and oligomers ultimately assemble into an ordered (2 × 2) hydrogen-bonded network structure prior to the formation of a multilayer solid water film. The results highlight a delicate balance that exists in water adlayers on oxide surfaces where hydrogen bonding may play an important role in stabilizing particular structures.

Hydroxylation of thin oxide films

The examples discussed so far refer to water adsorption to bulk-like thin films (i.e., films of reasonable thickness and structural similarity to the corresponding bulk oxides) at UHV conditions, where no structural modifications of the oxide lattice take place during adsorption. For complete hydroxylation of the oxide surfaces, which is expected to occur when environmentally more realistic water partial pressure conditions (mbar range) or higher water coverages are approached,

reactions between water and the oxide surfaces have to be considered as well. For the more ionic oxides in particular, this may involve hydrolysis of cation–anion bonds and strong structural modifications. The hydroxylation of MgO and CaO single-crystal surfaces and the partial transformation into the corresponding hydroxide as a function of relative humidity have been studied by ambient pressure XPS. Those studies revealed that the CaO(001) surface gets fully hydroxylated even under UHV conditions and transforms into the hydroxide, involving hydroxylation of the subsurface regions, at elevated water partial pressure [92]. On the other hand, a certain threshold water pressure in the sub-mbar range has to be applied to achieve sufficient surface hydroxylation of MgO(001) [93]. Studies on the corresponding thin film surfaces confirmed these results. Figure 11(a) compares STM images of the surface of a clean CaO(001) film (top) and after a saturation dose of water under UHV conditions at room temperature (bottom) [77, 79]. Clearly, water adsorption leads to strong structural modification of the surface, which is due to complete surface hydroxylation and partial solvation of Ca^{2+} ions. The latter can in part be explained by the sufficiently large structural flexibility of the CaO lattice, which allows easy rupture of cation–anion bonds.

By contrast, hydroxylation of thick, bulk-like MgO(001) films at room temperature and at UHV conditions is limited to defect sites, and to obtain complete hydroxylation, a threshold water partial pressure of about 0.01 mbar has to be applied [Fig. 10(b)] [94]. Titration of Mg^{2+} sites with CO has shown that the number of low-coordinated Mg^{2+} sites gets strongly enhanced upon hydroxylation, suggesting the occurrence of similar structural modifications as in the case of CaO(001). Interestingly, the threshold pressure for hydroxylation decreases by 3 orders of magnitude as the film thickness is

reduced from 12 ML to 2 ML [Fig. 10(b)] [94]. This effect is not related to an increased abundance of defects on the ultrathin film, but can be explained by a decreased energetic barrier for the rupture of $\text{Mg}^{2+}-\text{O}^{2-}$ bonds, which is related to the greater structural flexibility of the MgO lattice in the ultrathin regime [95].

Polar oxide surfaces are intrinsically reactive toward water because surface hydroxyls provide compensating charges necessary to remove polarity. Also, in polar oxide films grown on metal substrates, where the compensating charge density at the metal–oxide interface is readily provided by the metal, the free film surface needs to be compensated by conventional mechanisms, e.g., surface hydroxylation. Conversely, the thinnest oxide films (monolayers) are intrinsically nonpolar, thus reducing their activity toward water. In fact, the FeO(111) monolayer film is stable in pure water vapor environment, as shown by the O 1s XP spectrum obtained after exposure to 1 mbar water vapor. The latter exhibits only one component attributable to the lattice oxygen species, and no further contribution from hydroxyls [Fig. 12(a), (i) and (ii)] [96]. In addition, the structural integrity of the FeO(111) monolayer appears to be maintained upon exposure to air ambient and even liquid water, as shown by the STM images presented in Fig. 12(c), where the long-range ordered Moiré superlattice characteristic of FeO(111)/Pt(111) is proved to persist in the corresponding environment.

Exposure of FeO(111) to a high-pressure oxygen atmosphere leads to a transformation of the FeO bilayer to a O–Fe–O trilayer [97, 98, 99]. Both the additional oxygen incorporated in the film, which shows up in XPS as a shoulder on the high binding energy side of the main O 1s component, and the similarity of the STM appearance suggest that this transformation occurs also upon exposure of the FeO film to air [Fig. 12(a), (iii) and (iv)]. In addition, the IRA spectrum of an air-exposed film reveals the presence of hydroxyl species with characteristic vibrations at 3650 cm^{-1} [Fig. 12(b)]. It can, therefore, be concluded that the trilayer structure is highly active in water dissociation. As a result, an O–Fe–OH trilayer is formed [Fig. 12(d)] and the additional O 1s signal in XPS can be attributed to hydroxyl species [96]. XPS quantification reveals a maximum hydroxyl coverage of 0.45 ML. Together with the ordered appearance in STM, this suggests that the hydroxylation activity is restricted to the most reactive region within the Moiré unit cell, which, according to DFT calculations, is the Fe-hcp region [97].

All UHV-based, well-defined silica models have a common structural motif, which consists of corner-sharing $[\text{SiO}_4]$ tetrahedra arranged in a honeycomb structure (section “Silica film”) [100]. The fact that the surfaces are terminated by siloxane bonds renders the regular parts of the films

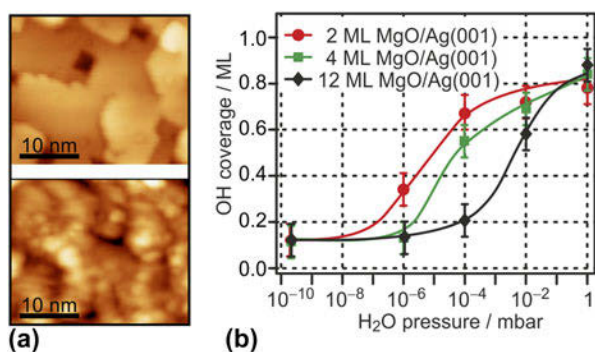


Figure 11: (a) STM images ($30 \times 25\text{ nm}^2$) of 10 ML CaO(001)/Mo(001) (top) and of the same surface exposed to a saturation dose of water at room temperature (bottom). (Reprinted with permission from Ref. 79. Copyright (2016) American Chemical Society.) (b) H₂O pressure-dependent surface hydroxyl coverage on Ag(001)-supported MgO(001) films of different thickness. (Reprinted with permission from Ref. 94. Copyright (2010) American Chemical Society.)

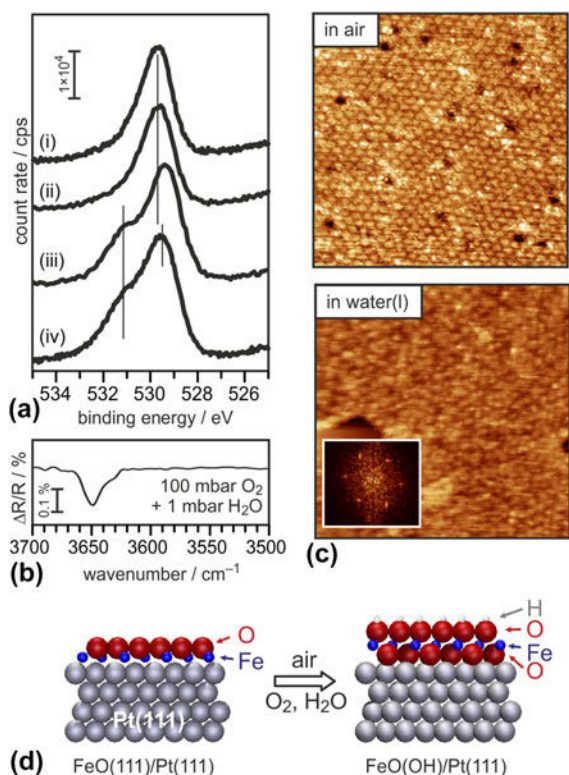


Figure 12: (a) O 1s XP spectra, from top to bottom, of (i) clean FeO(111)/Pt(111), the film exposed to (ii) 1 mbar D_2O , (iii) air, and (iv) 100 mbar O_2 and 1 mbar H_2O . (b) IR spectrum of the FeO(111)/Pt(111) film exposed to 100 mbar O_2 and 1 mbar H_2O . (c) Ambient-STM images ($60 \times 60 \text{ nm}^2$) of the FeO(111)/Pt(111) film in air (top) and in liquid water (bottom). (Reprinted with permission from Ref. 96. Copyright (2011) American Chemical Society.) (d) Model of the FeO(111)/Pt(111) film (left) and of the Pt-O-Fe-OH film (right) formed by exposure to air.

hydrophobic and, thus, unreactive toward water. Indeed, the silica bilayer on Ru(0001) can be exposed to air and pH-neutral aqueous solutions without any noticeable accompanying chemical and structural modifications to the film (see also section “Water-silica interface”). Hydroxylation of these model systems occurs only at defect sites, which, on well-prepared films, are scarce [101]. Since hydroxyl groups on silica (silanol groups) are of enormous importance for several technological applications, their creation and further utilization on well-defined model systems may help to obtain more fundamental insight into specific interfacial reactions where silanols are involved. Hydroxylation of the films could be achieved in the presence of water ice by the help of electron bombardment [102]. This is exemplified by the TPD spectra shown in Fig. 13(a), which have been obtained after dosing water (D_2O) at a substrate temperature of 100 K and followed by heating to RT (normal route, black curve), or with an additional electron bombardment prior to heating (electron-assisted route, red curve). The strong enhancement of water desorption from the electron-bombarded sample is related to a significantly increased abundance of D_2O and OD’s on the silica surface. More

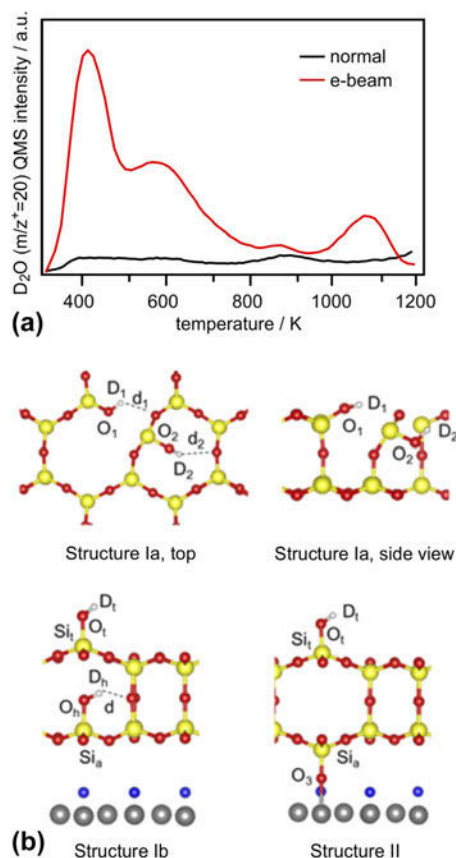


Figure 13: (a) TPD spectra ($m/z = 20$ amu) of SiO_2 samples exposed to 5 L D_2O at 100 K and then exposed (“e-beam,” red trace) or not exposed (“normal,” black trace) to an electron beam (0.05 mA, 200 eV, 60 s). (b) Hydroxylation structures for silica films involving breaking of in-plane (structure Ia, top) and vertical (structures Ib and II, bottom) siloxane bridges, obtained from DFT calculations. (Reprinted from Ref. 102—Published by the PCCP Owner Societies.)

specifically, the thermal route leads to the formation of isolated hydroxyl groups at defect sites within the film, which recombine at elevated temperature and desorb as molecular water at 900 K, and some additional hydrogen-bonded physisorbed water, which desorbs at lower temperatures ($< 500 \text{ K}$). The small amount of water desorbing from this sample supports the idea of the inert nature of the silica bilayer film surface. By contrast, enhanced hydroxylation of the electron-bombarded sample gives rise to much larger and more clearly defined water desorption peaks with maxima at 450 and 600 K, as well as an additional high-temperature desorption feature at $\sim 1070 \text{ K}$ [102, 103]. It is interesting to see that in terms of peak temperatures associated with individual desorption states, there is general agreement with analogous TPD spectra collected from hydroxylated bulk silica samples, which suggests the presence of similar water and hydroxyl species on the hydroxylated silica film. According to the Zhuravlev model [104], the desorption peaks are attributed to the following adsorption states and processes:

Chemisorbed molecular water gives rise to desorption at 400 K, whereas the high-temperature peaks are assigned to recombinative water desorption originating from vicinal (at 600 K) and isolated hydroxyls (above 800 K).

The creation of silanols requires the rupture of siloxane bridges, and several possibilities of how this could be achieved have been modeled by DFT [102]. As shown by the structural models presented in Fig. 13(b), rupture of an in-plane siloxane bridge results in two silanol groups, which are both engaged as donor groups in hydrogen bonds (structure Ia). On the other hand, breaking the Si–O–Si linkage between the two silicate layers results in one hydrogen-bonded silanol and one terminal silanol species (structure Ib). In addition to these processes, which are basically the same as assumed for bulk silica surfaces, the presence of the metallic substrate underneath the silica film opens the possibility for another mechanism, which involves hydrogen release and Ru oxidation (structure II). According to the computed hydroxylation energies and further experimental observations (D_2 desorption observed in TPD and infrared signals of terminal OD groups) [102], all three proposed structures are likely to be formed initially during electron bombardment or are created via transformation of one structure into another during heating to elevated temperature. Further experimental studies of the mechanism of electron-assisted hydroxylation of the silica films support the idea that the primary effect of electron irradiation is not the creation of defects (i.e., rupture of siloxane bridges) in the films, but the formation of reactive water radiolysis products (e.g., hydroxyl radicals) in the ice layer, which diffuse to the silica–ice interface and attack the siloxane bridges [103].

Stability and dissolution of thin oxide films in aqueous solutions

The investigations discussed so far were limited to systems studied under UHV conditions, which immediately poses the question how these results relate to oxide systems at ambient conditions such as an aqueous environment. In the following, we illustrate how such well-defined systems prepared under UHV conditions can be used to study the properties of oxide surfaces under ambient conditions. A variety of important technologies involve processes at the liquid–oxide interface. Aiming at the investigation of such processes using well-defined thin oxide films, the system has to be stable under the specific environmental conditions of interest. For surface science investigations in particular, it is desirable that the structural order is maintained. Since the chemical properties of (most) oxide thin films are similar to those of the corresponding bulk analogues, their stability and dissolution behavior is expected to follow the same trends. Dissolution rates for oxide thin film samples can be derived from the

measured decrease in film thickness upon exposure to aqueous solution, which can straightforwardly be determined from the intensities of the oxide and substrate XPS or AES emissions.

XP spectra (O 1s and Si 2p regions) taken after exposing bilayer SiO₂/Ru to deionized water at 90 °C, and NaOH(aq) at 25 °C for various times are displayed in Fig. 14(a) [103]. Clearly, deionized water (pH 7) does not affect the film structure to any significant extent, even at elevated temperature. While a small shift of all silica-related XP peaks to higher BE, which reflects a slight change in the electronic structure of the system (band bending), is noted, neither the Si 2p nor the O 1s peaks suffer any loss of intensity. In contrast, the intensity of both peaks decreases significantly, even at 25 °C, when the silica bilayer is exposed to alkaline media (NaOH, pH 13). The equal relative signal intensity loss of Si and O peaks observed with time of exposure allows to conclude that, in accordance with general experience, the dissolution process in alkaline media can be described as the OH[−]-catalyzed hydrolysis of SiO₂ (SiO₂ + 2H₂O → H₄SiO₄). One can further state that the bilayer SiO₂/Ru films resemble the dissolution behavior of other, more abundant forms of silica (quartz, amorphous silica), which are found to be practically insoluble in the neutral pH range, yet strongly soluble in alkaline conditions. From more systematic studies [Fig. 14(b)], it is clear that removal of SiO₂ from the sample occurs faster at higher temperature and pH, which is also qualitatively consistent with the behavior noted from bulk-phase silica analogues [105]. The dissolution rates for the thin film sample can be modeled by the general silica dissolution rate model derived by Bickmore et al. [105], which accounts for variations in pH, temperature, and the coverage of neutral ($\theta_{\text{Si-OH}}$) and deprotonated ($\theta_{\text{Si-O}^-}$) silanols. Because the silica film is hydrophobic and lacks significant initial silanol coverage, the latter two contributions can be neglected and the rate equation simplifies to:

$$\frac{d\text{Si}}{dt}/\text{mol/s} = e^{6.7 \pm 1.8} \text{T}e^{\left(\frac{-77.5 \pm 6.0}{RT}\right)} [\text{OH}^-] \quad .$$

A comparison of the dissolution rates predicted from that relation to those estimated on the basis of the initial rates of Si XPS peak attenuations from the thin films shows good agreement between the model and the experiment [103]. From this, it is concluded that dissolution of the film in alkaline media is initiated by OH[−] attack at Si centers. Note that this leads to a rupture of siloxane bonds. Thus, the initial step in the dissolution process can qualitatively be described by models that are similar to those used to explain electron-assisted hydroxylation of the silica film [Fig. 13(b)]. In general, the silica bilayer films were found to be stable (i.e.,

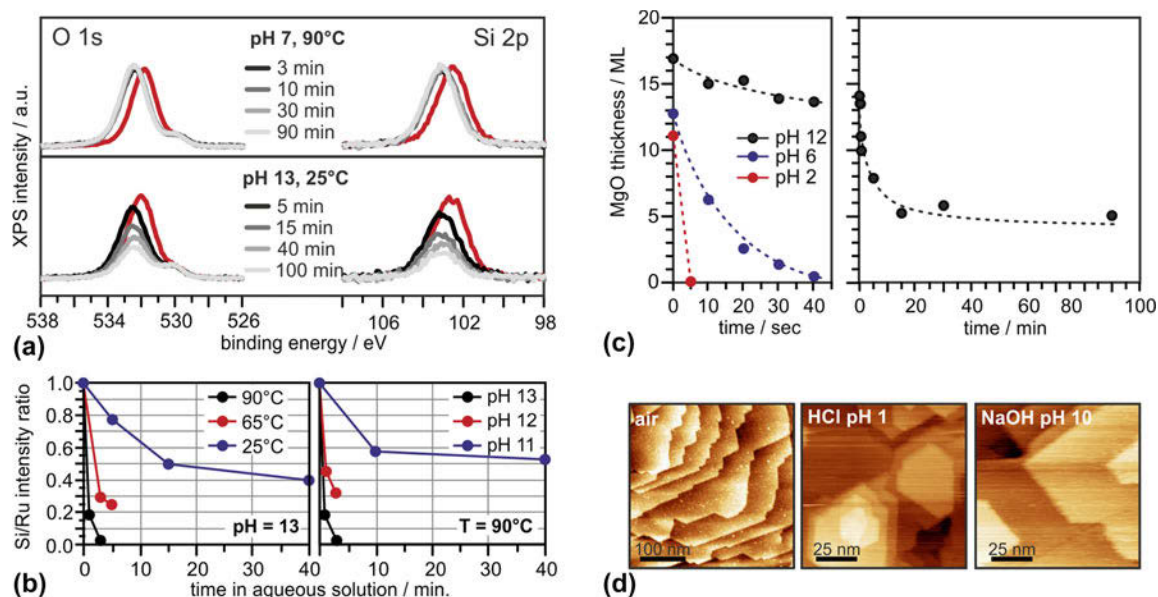


Figure 14: (a) Evolution of O 1s (left) and Si 2p (right) XP spectra of SiO₂/Ru(0001) samples as a function of time of exposure to (top) deionized water at 90 °C, and (bottom) 0.1 M NaOH at 25 °C. (b) Peak intensity ratios of Si 2p relative to Ru 3d for bilayer SiO₂/Ru samples exposed to aqueous NaOH solutions at pH 13 and various temperatures (blue = 25 °C, red = 65 °C, and black = 90 °C; left) and varying pH (blue = 11, red = 12, and black = 13) at 90 °C (right) as a function of time spent within the aqueous environments. (Adapted from Ref. 103.) (c) (left) Dissolution of MgO(001)/Ag(001) films (initial thicknesses corresponding to the values at time = 0 s) in various environments plotted as MgO film thickness versus time of exposure to solutions; black: 0.01 M NaOH solution (pH 12), blue: Millipore water (pH 6), red: 0.01 M HCl solution (pH 2). (right) Dissolution of MgO(001)/Ag(001) in 0.01 M NaOH. (Reprinted from Ref. 106, Copyright (2014), with permission from Elsevier.) (d) Ambient STM images of Fe₃O₄(111)/Pt(111) taken after transfer from UHV to air (left), after 60-min exposure to 0.1 M HCl, pH 1 (middle) and after 60-min exposure to NaOH_{aq}, pH 10 (right).

negligible dissolution rates) at room temperature in acidic and neutral aqueous solutions and in alkaline media up to pH 10 [103].

MgO is a basic oxide [point of zero charge (PZC) in the pH 10 range] and therefore expected to be more stable in alkaline media than in neutral and acidic environment [107]. Results of dissolution experiments performed with MgO(001)/Ag(001) thin films are presented in Fig. 14(c), where the variation in MgO film thickness as a function of time is displayed for exposure to acidic (pH 2, 0.01 M HCl), alkaline (pH 12, 0.01 M NaOH), and close-to-neutral (pH 6, Millipore water) environments, respectively [106]. The data shown in Fig. 14(c) are consistent with the expected faster dissolution of MgO in acidic media. In fact, in 0.01 M HCl solution the dissolution is so fast that a 11 ML thick film was completely dissolved within the first 5 s of exposure. The dissolution rate is smaller at pH 6; however, even under these conditions a 13 ML thin MgO film was completely dissolved within 40 s of exposure. During the same period, only 3 ML MgO was dissolved from the MgO sample upon exposure to alkaline (pH 12) solutions. For the latter, the dissolution behavior was studied for prolonged exposures (up to 90 min), the results of which show that the dissolution is initially fast and considerably slows down with time, until a stable surface state is obtained after 20–30 min of exposure. This suggests the formation of a brucite (Mg(OH)₂)-

like passivating surface layer during exposure to alkaline solution, for which the dissolution rate is considerably smaller than for MgO [108]. Because of the partial dissolution, and transformation of the surface layers into a hydroxide, MgO films exposed to alkaline media are subject to strong restructuring. Even if the crystallinity of the films can partially be recovered by annealing at elevated temperature, the initial structure of the MgO(001) films cannot be restored [106].

Iron oxides are, according to the corresponding Fe–water Pourbaix diagram, stable in aqueous solutions in a wide range of pH. Thus, it is not surprising that also thin iron oxide films are very stable in aqueous solutions. As an example, STM images taken in air from Fe₃O₄(111)/Pt(111) films, which have been prepared in UHV, subsequently transferred to air and exposed to aqueous solutions (pH 1, 0.1 M HCl and pH 10, NaOH_{aq}) for 1 h, are shown in Fig. 14(d) [109, 110]. These images reveal that the island–terrace–step structure of the thin film remains intact. Furthermore, the step edges run straight along the crystallographically preferred directions and the terraces are atomically flat. XPS taken from the exposed films indicates a slight oxidation of the surface, but this does obviously not lead to large structural modifications. Both Fe₃O₄(111)/Pt(111) and bilayer silica films [and to a limited extent also MgO(001)/Ag(001)] are therefore well suited for further investigations of processes involving oxide–liquid interfaces.

Water–silica interface

To date, most of the research on silica bilayers has been performed in idealized ultrahigh vacuum environments. These conditions provide a high degree of experimental control which enables unambiguous structural assessment. Yet real-world applications of silica and its derivatives demand higher pressures and temperatures and occur under ambient conditions. Recent research on silica bilayers beyond ultrahigh vacuum addresses these practical considerations by bridging the gap between UHV and ambient.

To bridge such gap, the structure of silica has been investigated with high-resolution liquid atomic force microscopy (AFM). Silica films are grown in UHV and subsequently transferred through ambient to the liquid environment (400 mM NaCl solution). Figure 15 shows images of the bilayer silica structure attained with ultrahigh vacuum STM [Fig. 15(a)] and high-resolution liquid AFM [Fig. 15(b)] [111]. The low-temperature UHV STM image exhibits atomic resolution of the silica structure while the resolution of the room-temperature liquid AFM images allows identifying the ring structures. The structures appear remarkably similar as confirmed quantitatively from pair distribution functions of the ring center positions. These results show that the silica film is structurally robust against ambient and aqueous conditions; this result is consistent with the conclusions of the previous study which found the silica bilayer film to be exceptionally stable against hydroxylation [102]. In contrast, many UHV surface structures are not stable under ambient conditions due to unsaturated bonds [96, 106]. The stability of the silica bilayer makes it an optimal playground to test the resolution of liquid AFM as the amorphous structure circumvents the common challenge of distinguishing between true atomic resolution and lattice resolution [112]. Furthermore, establishing the stability of the silica bilayer under ambient conditions opens the door to future device applications.

Conclusions

In this review article, we highlighted recent results obtained from surface science investigations for the interaction of water with metal-supported crystalline thin oxide films, which represent versatile models of the corresponding bulk oxides and can additionally provide access to experimental techniques that cannot easily be applied to realistic systems. We have discussed several aspects of water–oxide interactions at different levels of complexity, from the formation of ordered superstructures and the hydroxylation of oxide surfaces, to the stability and dissolution of oxides in aqueous solutions. It has been demonstrated, at least for simple model systems, that molecular-level understanding of the structure of water at

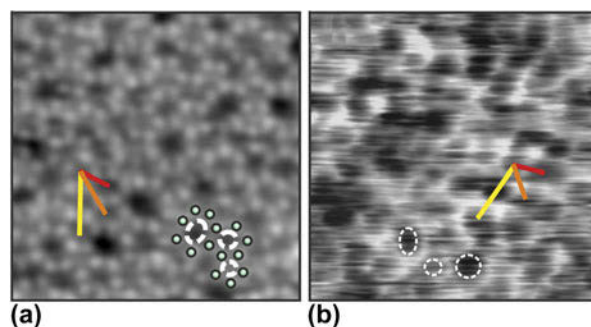


Figure 15: An amorphous silica bilayer film with atomic resolution of silicon atoms by STM in UHV (a) and ring resolution by liquid AFM in (b). Both images have a scan frame of 5×5 nm. Red, orange, and yellow measurement bars show examples of ring center–center distances for the first three families of ring neighbors identified in the amorphous silica bilayer. Several individual rings are marked in each image [111].

oxide surfaces can be obtained by combining surface science spectroscopic and microscopic methods with support from computational modeling. Specifically for the alkaline earth metal oxides, this combination of methods allowed us to identify different ordered water–hydroxyl superstructures, such as the two-dimensional structures on MgO(001) and the one-dimensional chain structure on CaO(001), and to explain the stability of the various structures based on the properties of the substrate (basicity, lattice constant), the corresponding water–substrate interaction strength, and the ability to form hydrogen bonded networks. The latter is also important in the formation of the (2×2) water superstructure observed on Fe₃O₄(111). In this case, water molecules initially dissociate to form OH_r–O_sH pairs. Those act as nuclei for dimer formation by attachment of molecular water, from which, by maximizing the number of hydrogen bonds, an ordered (2×2) superstructure forms.

In contrast to the cases described above, the surface of the silica bilayer film is rather unreactive toward water because of the presence of completely saturated Si⁴⁺ ions. Hydroxylation is only achieved by providing additional energy input, e.g., through electron bombardment of an ice layer adsorbed on top of the silica surface. The different kinds of surface silanol groups formed in this way have essentially the same properties as those present on hydroxylated silica powder. Formation of stable hydroxyls requires, however, the rupture of substrate silicon–oxygen bonds (hydrolysis). In particular for the more ionic oxides such as the alkaline earth oxides, hydrolysis leads to strong morphological modifications of the surface, which significantly increases the structural complexity of the systems. Although some progress has been achieved in the description of the more complex water–oxide systems, including the dynamic aqueous–oxide interface, understanding the processes occurring at the interfaces of such systems at the molecular level still represent an enormous challenge.

References

1. P.A. Thiel and T.E. Madey: The interaction of water with solid surfaces—Fundamental aspects. *Surf. Sci. Rep.* **7**, 211 (1987).
2. M.A. Henderson: The interaction of water with solid surfaces: Fundamental aspects revisited. *Surf. Sci. Rep.* **46**, 1 (2002).
3. A. Verduguer, G.M. Sacha, H. Bluhm, and M. Salmeron: Molecular structure of water at interfaces: Wetting at the nanometer scale. *Chem. Rev.* **106**, 1478 (2006).
4. G.E. Ewing: Ambient thin film water on insulator surfaces. *Chem. Rev.* **106**, 1511 (2006).
5. G.E. Brown, V.E. Henrich, W.H. Casey, D.L. Clark, C. Eggleston, A. Felmy, D.W. Goodman, M. Grätzel, G. Maciel, M.I. McCarthy, K.H. Nealsen, D.A. Sverjensky, M.F. Toney, and J.M. Zachara: Metal oxide surfaces and their interactions with aqueous solutions and microbial organisms. *Chem. Rev.* **99**, 77 (1999).
6. E. Bjornehohn, M.H. Hansen, A. Hodgson, L.M. Liu, D. T. Limmer, A. Michaelides, P. Pedevilla, J. Rossmeisl, H. Shen, G. Tocci, E. Tyrode, M.M. Walz, J. Werner, and H. Bluhm: Water at interfaces. *Chem. Rev.* **116**, 7698 (2016).
7. A. Hodgson and S. Haq: Water adsorption and the wetting of metal surfaces. *Surf. Sci. Rep.* **64**, 381 (2009).
8. J. Carrasco, A. Hodgson, and A. Michaelides: A molecular perspective of water at metal interfaces. *Nat. Mater.* **11**, 667 (2012).
9. R.R. Rao, M.J. Kolb, J. Hwang, A.F. Pedersen, A. Mehta, H. You, K.A. Stoerzinger, Z.X. Feng, H. Zhou, H. Bluhm, L. Giordano, I.E.L. Stephens, and Y. Shao-Horn: Surface orientation dependent water dissociation on rutile ruthenium dioxide. *J. Phys. Chem. C* **122**, 17802 (2018).
10. M. Schwarz, F. Faisal, S. Mohr, C. Hohner, K. Werner, T. Xu, T. Skala, N. Tsud, K.C. Prince, V. Matolin, Y. Lykhach, and J. Libuda: Structure-dependent dissociation of water on cobalt oxide. *J. Phys. Chem. Lett.* **9**, 2763 (2018).
11. X.L. Hu, J. Carrasco, J. Klimes, and A. Michaelides: Trends in water monomer adsorption and dissociation on flat insulating surfaces. *Phys. Chem. Chem. Phys.* **13**, 12447 (2011).
12. R.T. Mu, Z.J. Zhao, Z. Dohnalek, and J.L. Gong: Structural motifs of water on metal oxide surfaces. *Chem. Soc. Rev.* **46**, 1785 (2017).
13. M. Meier, J. Hulva, Z. Jakub, J. Pavelec, M. Setvin, R. Bliem, M. Schmid, U. Diebold, C. Franchini, and G.S. Parkinson: Water agglomerates on Fe₃O₄(001). *Proc. Natl. Acad. Sci. U. S. A* **115**, E5642 (2018).
14. R. Włodarczyk, M. Sierka, K. Kwapien, J. Sauer, E. Carrasco, A. Aumer, J.F. Gomes, M. Sterrer, and H.-J. Freund: Structures of the ordered water monolayer on MgO(001). *J. Phys. Chem. C* **115**, 6764 (2011).
15. P. Fenter and N.C. Sturchio: Mineral-water interfacial structures revealed by synchrotron X-ray scattering. *Prog. Surf. Sci.* **77**, 171 (2004).
16. J. Heidberg, B. Redlich, and D. Wetter: Adsorption of water vapor on the MgO(100) single-crystal surface. *Ber. Bunsenges. Phys. Chem.* **99**, 1333 (1995).
17. B. Meyer, D. Marx, O. Dulub, U. Diebold, M. Kunat, D. Langenberg, and C. Wöll: Partial dissociation of water leads to stable superstructures on the surface of zinc oxide. *Angew. Chem., Int. Ed.* **43**, 6642 (2004).
18. I.M. Brookes, C.A. Muryn, and G. Thornton: Imaging water dissociation on TiO₂(110). *Phys. Rev. Lett.* **87**, 266103 (2001).
19. J. Balajka, M.A. Hines, W.J.I. DeBenedetti, M. Komora, J. Pavelec, M. Schmid, and U. Diebold: High-affinity adsorption leads to molecularly ordered interfaces on TiO₂ in air and solution. *Science* **361**, 786 (2018).
20. U. Diebold: The surface science of titanium dioxide. *Surf. Sci. Rep.* **48**, 53 (2003).
21. G.A. Kimmel, M. Baer, N.G. Petrik, J. VandeVondele, R. Rousseau, and C.J. Mundy: Polarization- and azimuth-resolved infrared spectroscopy of water on TiO₂(110): Anisotropy and the hydrogen-bonding network. *J. Phys. Chem. Lett.* **3**, 778 (2012).
22. N.G. Petrik and G.A. Kimmel: Reaction kinetics of water molecules with oxygen vacancies on rutile TiO₂(110). *J. Phys. Chem. C* **119**, 23059 (2015).
23. Y.M. Wang and C. Wöll: IR spectroscopic investigations of chemical and photochemical reactions on metal oxides: Bridging the materials gap. *Chem. Soc. Rev.* **46**, 1875 (2017).
24. H.J. Freund, H. Kuhlenbeck, and V. Staemmler: Oxide surfaces. *Rep. Prog. Phys.* **59**, 283 (1996).
25. C.T. Campbell: Ultrathin metal films and particles on oxide surfaces: Structural, electronic and chemisorption properties. *Surf. Sci. Rep.* **27**, 1 (1997).
26. F.P. Netzer and A. Fortunelli, eds.: *Oxide Materials at the Two-dimensional Limit*, Springer Series in Materials Science, Vol. 234 (Springer, Switzerland, 2016).
27. N. Niliius: Properties of oxide thin films and their adsorption behavior studied by scanning tunneling microscopy and conductance spectroscopy. *Surf. Sci. Rep.* **64**, 595 (2009).
28. S. Surnev, M.G. Ramsey, and F.P. Netzer: Vanadium oxide surface studies. *Prog. Surf. Sci.* **73**, 117 (2003).
29. G. Kresse, M. Schmid, E. Napetschnig, M. Shishkin, L. Köhler, and P. Varga: Structure of the ultrathin aluminum oxide film on NiAl(110). *Science* **308**, 1440 (2005).
30. C.R. Henry: Surface studies of supported model catalysts. *Surf. Sci. Rep.* **31**, 231 (1998).
31. S. Schintke, S. Messerli, M. Pivetta, F. Patthey, L. Libioulle, M. Stengel, A. De Vita, and W.-D. Schneider: Insulator at the ultrathin limit: MgO on Ag(001). *Phys. Rev. Lett.* **87**, 276801 (2001).
32. M. Klaua, D. Ullmann, J. Barthel, W. Wulfhekel, J. Kirschner, R. Urban, T.L. Monchesky, A. Enders, J.F. Cochran, and B. Heinrich: Growth, structure, electronic, and magnetic

- properties of MgO/Fe(001) bilayers and Fe/MgO/Fe(001) trilayers. *Phys. Rev. B* **64**, 134411 (2001).
33. **M.C. Wu, J.S. Corneille, C.A. Estrada, J.W. He, and D. W. Goodman:** Synthesis and characterization of ultra-thin MgO films on Mo(100). *Chem. Phys. Lett.* **182**, 472 (1991).
 34. **S. Benedetti, H.M. Benia, N. Nilius, S. Valeri, and H.J. Freund:** Morphology and optical properties of MgO thin films on Mo(001). *Chem. Phys. Lett.* **430**, 330 (2006).
 35. **X. Shao, P. Myrach, N. Nilius, and H.J. Freund:** Growth and morphology of calcium-oxide films grown on Mo(001). *J. Phys. Chem. C* **115**, 8784 (2011).
 36. **N. Nilius, S. Benedetti, Y. Pan, P. Myrach, C. Noguera, L. Giordano, and J. Goniakowski:** Electronic and electrostatic properties of polar oxide nanostructures: MgO(111) islands on Au(111). *Phys. Rev. B* **86**, 205410 (2012).
 37. **J. Goniakowski, C. Finocchi, and C. Noguera:** Polarity of oxide surfaces and nanostructures. *Rep. Prog. Phys.* **71**, 016501 (2008).
 38. **F. Finocchi, A. Barbier, J. Jupille, and C. Noguera:** Stability of rocksalt (111) polar surfaces: Beyond the octopole. *Phys. Rev. Lett.* **92**, 136101 (2004).
 39. **J. Pal, M. Smerieri, E. Celasco, L. Savio, L. Vattuone, and M. Rocca:** Morphology of monolayer MgO films on Ag(100): Switching from corrugated islands to extended flat terraces. *Phys. Rev. Lett.* **112**, 126102 (2014).
 40. **J. Pal, M. Smerieri, E. Celasco, L. Savio, L. Vattuone, R. Ferrando, S. Tosoni, L. Giordano, G. Pacchioni, and M. Rocca:** How growing conditions and interfacial oxygen affect the final morphology of MgO/Ag(100) films. *J. Phys. Chem. C* **118**, 26091 (2014).
 41. **K.P. McKenna and A.L. Shluger:** Electron-trapping polycrystalline materials with negative electron affinity. *Nat. Mater.* **7**, 859 (2008).
 42. **S. Benedetti, P. Torelli, S. Valeri, H.M. Benia, N. Nilius, and G. Renaud:** Structure and morphology of thin MgO films on Mo (001). *Phys. Rev. B* **78**, 195411 (2008).
 43. **S. Benedetti, F. Stavale, S. Valeri, C. Noguera, H.J. Freund, J. Goniakowski, and N. Nilius:** Steering the growth of metal ad-particles via interface interactions between a MgO thin film and a Mo support. *Adv. Funct. Mater.* **23**, 75 (2013).
 44. **L. Giordano, F. Cinquini, and G. Pacchioni:** Tuning the surface metal work function by deposition of ultrathin oxide films: Density functional calculations. *Phys. Rev. B* **73**, 045414 (2006).
 45. **H.M. Benia, P. Myrach, N. Nilius, and H.J. Freund:** Structural and electronic characterization of the MgO/Mo(001) interface using STM. *Surf. Sci.* **604**, 435 (2010).
 46. **M. Sterrer, E. Fischbach, T. Risse, and H-J. Freund:** Geometric characterization of a singly charged oxygen vacancy on a single-crystalline MgO(001) film by electron paramagnetic resonance spectroscopy. *Phys. Rev. Lett.* **94**, 186101 (2005).
 47. **M. Sterrer, E. Fischbach, M. Heyde, N. Nilius, H.P. Rust, T. Risse, and H.J. Freund:** Electron paramagnetic resonance and scanning tunneling microscopy investigations on the formation of F^+ and F^0 color centers on the surface of thin MgO(001) films. *J. Phys. Chem. B* **110**, 8665 (2006).
 48. **X. Shao, N. Nilius, P. Myrach, H.J. Freund, U. Martinez, S. Prada, L. Giordano, and G. Pacchioni:** Strain-induced formation of ultrathin mixed-oxide films. *Phys. Rev. B* **83**, 245407 (2011).
 49. **Y. Cui, X. Shao, M. Baldofski, J. Sauer, N. Nilius, and H. J. Freund:** Adsorption, activation, and dissociation of oxygen on doped oxides. *Angew. Chem., Int. Ed.* **52**, 11385 (2013).
 50. **S. Sastry, P.G. Debenedetti, and F.H. Stillinger:** Signatures of distinct dynamical regimes in the energy landscape of a glass-forming liquid. *Nature* **393**, 554 (1998).
 51. **R. Zallen:** *The Physics of Amorphous Solids* (Wiley-VCH Verlag GmbH & Co. KGaA, Weinheim, 2004).
 52. **L. Berthier and G. Biroli:** Theoretical perspective on the glass transition and amorphous materials. *Rev. Mod. Phys.* **83**, 587 (2011).
 53. **J.C. Mauro and E.D. Zanotto:** Two centuries of glass research: Historical trends, current status, and grand challenges for the future. *Int. J. Appl. Glass Sci.* **5**, 313 (2014).
 54. **W.H. Zachariasen:** The atomic arrangement in glass. *J. Am. Chem. Soc.* **54**, 3841 (1932).
 55. **L. Lichtenstein, M. Heyde, and H-J. Freund:** Atomic arrangement in two-dimensional silica: From crystalline to vitreous structures. *J. Phys. Chem. C* **116**, 20426 (2012).
 56. **D. Löffler, J.J. Uhlrich, M. Baron, B. Yang, X. Yu, L. Lichtenstein, L. Heinke, C. Büchner, M. Heyde, S. Shaikhutdinov, H-J. Freund, R. Włodarczyk, M. Sierka, and J. Sauer:** Growth and structure of crystalline silica sheet on Ru (0001). *Phys. Rev. Lett.* **105**, 146104 (2010).
 57. **L. Lichtenstein, C. Büchner, B. Yang, S. Shaikhutdinov, M. Heyde, M. Sierka, R. Włodarczyk, J. Sauer, and H-J. Freund:** The atomic structure of a metal-supported vitreous thin silica film. *Angew. Chem., Int. Ed.* **51**, 404 (2012).
 58. **L. Lichtenstein, M. Heyde, and H-J. Freund:** Crystalline-vitreous interface in two dimensional silica. *Phys. Rev. Lett.* **109**, 106101 (2012).
 59. **X. Yu, B. Yang, J.A. Boscoboinik, S. Shaikhutdinov, and H-J. Freund:** Support effects on the atomic structure of ultrathin silica films on metals. *Appl. Phys. Lett.* **100**, 151608 (2012).
 60. **P.Y. Huang, S. Kurasch, A. Srivastava, V. Skakalova, J. Kotakoski, A.V. Krasheninnikov, R. Hovden, Q. Mao, J. C. Meyer, J. Smet, D.A. Muller, and U. Kaiser:** Direct imaging of a two-dimensional silica glass on graphene. *Nano Lett.* **12**, 1081 (2012).
 61. **E.I. Altman and U.D. Schwarz:** Structural and electronic heterogeneity of two-dimensional amorphous silica layers. *Adv. Mater. Interfaces* **1**, 1400108 (2014).
 62. **R.M. Cornell and U. Schwertmann:** *The Iron Oxides* (Wiley-VCH Verlag GmbH & Co. KGaA, Weinheim, 2004); pp. 1–7.

63. G. Ertl, H. Knözinger, F. Schueth, and J. Weitkamp, eds.: *Handbook of Heterogeneous Catalysis*, Vol. 2, compl. rev. and enlarged ed. (WILEY-VCH Verlag GmbH & Co. KGaA, Weinheim, 2008).
64. R. Zboril, M. Mashlan, and D. Petridis: Iron(III) oxides from thermal processes: Synthesis, structural and magnetic properties, Mössbauer spectroscopy characterization, and applications. *Chem. Mater.* **14**, 969 (2002).
65. W. Weiss and W. Ranke: Surface chemistry and catalysis on well-defined epitaxial iron-oxide layers. *Prog. Surf. Sci.* **70**, 1 (2002).
66. N.G. Condon, F.M. Leibsle, T. Parker, A.R. Lennie, D. J. Vaughan, and G. Thornton: Biphasic ordering on Fe₃O₄(111). *Phys. Rev. B* **55**, 15885 (1997).
67. A. Barbieri, W. Weiss, M.A.V. Hove, and G.A. Somorjai: Magnetite Fe₃O₄(111): Surface structure by LEED crystallography and energetics. *Surf. Sci.* **302**, 259 (1994).
68. G.S. Parkinson: Iron oxide surfaces. *Surf. Sci. Rep.* **71**, 272 (2016).
69. A. Sala, H. Marchetto, Z.H. Qin, S. Shaikhutdinov, T. Schmidt, and H-J. Freund: Defects and inhomogeneities in Fe₃O₄(111) thin film growth on Pt(111). *Phys. Rev. B* **86**, 155430 (2012).
70. M. Melzer, J. Urban, H. Sack-Kongehl, K. Weiss, H-J. Freund, and R. Schlögl: Preparation of vanadium and vanadium oxide clusters by means of inert gas aggregation. *Catal. Lett.* **81**, 219 (2002).
71. W. Weiss and M. Ritter: Metal oxide heteroepitaxy: Stranski-Krastanov growth of iron oxides on Pt(111). *Phys. Rev. B* **59**, 5201 (1999).
72. D.T. Margulies, F.T. Parker, M.L. Rudee, F.E. Spada, J.N. Chapman, P.R. Aitchison, and A.E. Berkowitz: Origin of the anomalous magnetic behavior in single crystal Fe₃O₄ films. *Phys. Rev. Lett.* **79**, 5201 (1997).
73. M. Ritter and W. Weiss: Fe₃O₄(111) surface structure determined by LEED crystallography. *Surf. Sci.* **432**, 81 (1999).
74. S.K. Shaikhutdinov, M. Ritter, X.G. Wang, H. Over, and W. Weiss: Defect structures on epitaxial Fe₃O₄(111) films. *Phys. Rev. B* **60**, 11062 (1999).
75. C. Lemire, R. Meyer, V.E. Henrich, S. Shaikhutdinov, and H.J. Freund: The surface structure of Fe₃O₄(111) films as studied by CO adsorption. *Surf. Sci.* **572**, 103 (2004).
76. X. Li, J. Paier, J. Sauer, F. Mirabella, E. Zaki, F. Ivars-Barceló, S. Shaikhutdinov, and H.J. Freund: Surface termination of Fe₃O₄(111) films studied by CO adsorption revisited. *J. Phys. Chem. B* **122**, 527 (2018).
77. X. Zhao, X. Shao, Y. Fujimori, S. Bhattacharya, L.M. Ghiringhelli, H-J. Freund, M. Sterrer, N. Nilius, and S.V. Levchenko: Formation of water chains on CaO(001): What drives the 1D growth? *J. Phys. Chem. Lett.* **6**, 1204 (2015).
78. J. Carrasco, F. Illas, and N. Lopez: Dynamic ion pairs in the adsorption of isolated water molecules on alkaline-earth oxide (001) surfaces. *Phys. Rev. Lett.* **100**, 016101 (2008).
79. Y. Fujimori, X. Zhao, X. Shao, S.V. Levchenko, N. Nilius, M. Sterrer, and H-J. Freund: Interaction of water with the CaO (001) surface. *J. Phys. Chem. C* **120**, 5565 (2016).
80. D. Ferry, A. Glebov, V. Senz, J. Suzanne, J.P. Toennies, and H. Weiss: Observation of the second ordered phase of water on the MgO(100) surface: Low energy electron diffraction and helium atom scattering studies. *J. Chem. Phys.* **105**, 1697 (1996).
81. D. Halwidl, B. Stöger, W. Mayr-Schmölzer, J. Pavelec, D. Fobes, J. Peng, Z.Q. Mao, G.S. Parkinson, M. Schmid, F. Mittendorfer, J. Redinger, and U. Diebold: Adsorption of water at the SrO surface of ruthenates. *Nat. Mater.* **15**, 450 (2016).
82. Y.D. Kim, R.M. Lynden-Bell, A. Alavi, J. Stulz, and D.W. Goodman: Evidence for partial dissociation of water on flat MgO(100) surfaces. *Chem. Phys. Lett.* **352**, 318 (2002).
83. U. Leist, W. Ranke, and K. Al-Shamery: Water adsorption and growth of ice on epitaxial Fe₃O₄(111), FeO(111), and Fe₂O₃ (biphase). *Phys. Chem. Chem. Phys.* **5**, 2435 (2003).
84. Y. Joseph, C. Kuhrs, W. Ranke, M. Ritter, and W. Weiss: Adsorption of water on FeO(111) and Fe₃O₄(111): Identification of active sites for dissociation. *Chem. Phys. Lett.* **314**, 195 (1999).
85. Y. Joseph, W. Ranke, and W. Weiss: Water on FeO(111) and Fe₃O₄(111): Adsorption behavior on different surface terminations. *J. Phys. Chem. B* **104**, 3224 (2000).
86. P.A. Redhead: Thermal desorption of gases. *Vacuum* **12**, 203 (1962).
87. A.M. de Jong and J.W. Niemantsverdriet: Thermal desorption analysis: Comparative test of ten commonly applied procedures. *Surf. Sci.* **233**, 355 (1990).
88. F. Mirabella, E. Zaki, F. Ivars-Barceló, X. Li, J. Paier, J. Sauer, S. Shaikhutdinov, and H-J. Freund: Cooperative formation of long-range ordering in water ad-layers on Fe₃O₄(111). *Angew. Chem., Int. Ed.* **57**, 1409 (2017).
89. E. Habenschaden and J. Küppers: Evaluation of flash desorption spectra. *Surf. Sci. Lett.* **138**, L147 (1984).
90. S.L. Tait, Z. Dohnálek, C.T. Campbell, and B.D. Kay: *n*-alkanes on MgO(100). I. Coverage-dependent desorption kinetics of *n*-butane. *J. Chem. Phys.* **122**, 164707 (2005).
91. P. Dementyev, K-H. Dostert, F. Ivars-Barceló, C.P. O'Brien, F. Mirabella, S. Schauer mann, X. Li, J. Paier, J. Sauer, and H-J. Freund: Water interaction with iron oxides. *Angew. Chem., Int. Ed.* **54**, 13942 (2015).
92. P. Liu, T. Kendelewicz, G.E. Brown, G.A. Parks, and P. Pianetta: Reaction of water with vacuum-cleaved CaO(100) surfaces: An X-ray photoemission spectroscopy study. *Surf. Sci.* **416**, 326 (1998).
93. P. Liu, T. Kendelewicz, G.E. Gordon, and G.A. Parks: Reaction of water with MgO(100) surfaces. Part I: Synchrotron X-ray photoemission studies of low-defect surfaces. *Surf. Sci.* **412-13**, 287 (1998).

94. E. Carrasco, M.A. Brown, M. Sterrer, H.-J. Freund, K. Kwapien, M. Sierka, and J. Sauer: Thickness-dependent hydroxylation of MgO(001) thin films. *J. Phys. Chem. C* **114**, 18207 (2010).
95. L. Savio, E. Celasco, L. Vattuone, M. Rocca, and P. Senet: MgO/Ag(100): Confined vibrational modes in the limit of ultrathin films. *Phys. Rev. B* **67**, 075420 (2003).
96. F. Ringleb, Y. Fujimori, H.F. Wang, H. Ariga, E. Carrasco, M. Sterrer, H.J. Freund, L. Giordano, G. Pacchioni, and J. Goniakowski: Interaction of water with FeO(111)/Pt(111): Environmental effects and influence of oxygen. *J. Phys. Chem. C* **115**, 19328 (2011).
97. L. Giordano, M. Lewandowski, I.M.N. Groot, Y.N. Sun, J. Goniakowski, C. Noguera, S. Shaikhutdinov, G. Pacchioni, and H.J. Freund: Oxygen-induced transformations of an FeO(111) film on Pt(111): A combined DFT and STM study. *J. Phys. Chem. C* **114**, 21504 (2010).
98. Y.N. Sun, L. Giordano, J. Goniakowski, M. Lewandowski, Z. H. Qin, C. Noguera, S. Shaikhutdinov, G. Pacchioni, and H. J. Freund: The interplay between structure and CO oxidation catalysis on metal-supported ultrathin oxide films. *Angew. Chem., Int. Ed.* **49**, 4418 (2010).
99. Y.N. Sun, Z.H. Qin, M. Lewandowski, E. Carrasco, M. Sterrer, S. Shaikhutdinov, and H.J. Freund: Monolayer iron oxide film on platinum promotes low temperature CO oxidation. *J. Catal.* **266**, 359 (2009).
100. S. Shaikhutdinov and H.J. Freund: Ultrathin silica films on metals: The long and winding road to understanding the atomic structure. *Adv. Mater.* **25**, 49 (2013).
101. B. Yang, E. Emmez, W.E. Kaden, X. Yu, J.A. Boscoboinik, M. Sterrer, S. Shaikhutdinov, and H.-J. Freund: Hydroxylation of metal-supported sheet-like silica films. *J. Phys. Chem. C* **117**, 8336 (2013).
102. X. Yu, E. Emmez, Q. Pan, B. Yang, S. Pomp, W.E. Kaden, M. Sterrer, S. Shaikhutdinov, H.-J. Freund, I. Goikoetxea, R. Wlodarczyk, and J. Sauer: Electron stimulated hydroxylation of a metal supported silicate film. *Phys. Chem. Chem. Phys.* **18**, 3755 (2016).
103. W.E. Kaden, S. Pomp, M. Sterrer, and H.J. Freund: Insights into silica bilayer hydroxylation and dissolution. *Top. Catal.* **60**, 471 (2017).
104. L.T. Zhuravlev: The surface chemistry of amorphous silica. Zhuravlev model. *Colloids Surf., A* **173**, 1 (2000).
105. B.R. Bickmore, J.C. Wheeler, B. Bates, K.L. Nagy, and D.L. Eggett: Reaction pathways for quartz dissolution determined by statistical and graphical analysis of macroscopic experimental data. *Geochim. Cosmochim. Acta* **72**, 4521 (2008).
106. F. Ringleb, M. Sterrer, and H.-J. Freund: Preparation of Pd-MgO model catalysts by deposition of Pd from aqueous precursor solutions onto Ag(001)-supported MgO(001) thin films. *Appl. Catal., A* **474**, 186 (2014).
107. D.A. Vermilyea: Dissolution of MgO and Mg(OH)₂ in aqueous solutions. *J. Electrochem. Soc.* **116**, 1179 (1969).
108. O.S. Pokrovsky and J. Schott: Experimental study of brucite dissolution and precipitation in aqueous solutions: Surface speciation and chemical affinity control. *Geochim. Cosmochim. Acta* **68**, 31 (2004).
109. H.F. Wang, H. Ariga, R. Dowler, M. Sterrer, and H.J. Freund: Surface science approach to catalyst preparation—Pd deposition onto thin Fe₃O₄(111) films from PdCl₂ precursor. *J. Catal.* **286**, 1 (2012).
110. H.F. Wang, W.E. Kaden, R. Dowler, M. Sterrer, and H. J. Freund: Model oxide-supported metal catalysts—Comparison of ultrahigh vacuum and solution based preparation of Pd nanoparticles on a single-crystalline oxide substrate. *Phys. Chem. Chem. Phys.* **14**, 11525 (2012).
111. K.M. Burson, L. Gura, B. Kell, C. Büchner, A.L. Lewandowski, M. Heyde, and H.-J. Freund: Resolving amorphous solid-liquid interfaces by atomic force microscopy. *Appl. Phys. Lett.* **108**, 201602 (2016).
112. F.F. Abraham and I.P. Batra: Theoretical interpretation of atomic-force- microscope images of graphite. *Surf. Sci.* **209**, L125 (1989).